Design of sculptured SnS/g-C$_3$N$_4$ photocatalytic nanostructure for highly efficient and selective CO$_2$ conversion to methane

Hossam A.E. Omr [a,g], Raghunath Putikam [b], Mahmoud Kamal Hussien [d], Amr Sabbah [d],
Tsai-Yu Lin [e], Kuei-Hsien Chen [d,e], Heng-Liang Wu [e,f], Shien-Ping Feng [c], Ming-Chang Lin [b],
Hyeonseok Lee [a,*]

[a] *Department of Photonics, National Sun Yat-sen University, No. 70, Lien-Hai Rd, Kaohsiung 80424, Taiwan*
[b] *Department of Applied Chemistry, National Yang-Ming Chiao Tong University, Hsinchu 300093, Taiwan*
[c] *Department of Advanced Design and Systems Engineering, City University of Hong Kong, Tat Chee Avenue, Hong Kong*
[d] *Institute of Atomic and Molecular Sciences, Academia Sinica, Taipei 10617, Taiwan*
[e] *Center for Condensed Matter Sciences, National Taiwan University, Taipei 10617, Taiwan*
[f] *Center of Atomic Initiative for New Materials, National Taiwan University, Taipei 10617, Taiwan*
[g] *Department of Chemistry, Faculty of Science, Assiut University, Assiut 71516, Egypt*

ARTICLE INFO

ABSTRACT

Here, we demonstrate the SnS/g-C$_3$N$_4$ crystallized and nanostructured photocatalysts for efficient and selective CO$_2$ conversion to CH$_4$ by engineered thermal evaporation and the decoration of g-C$_3$N$_4$ through a simple dipping method, overcoming the limitation of bulk SnS-based photocatalysts. The SnS/g-C$_3$N$_4$ nanostructured photocatalysts exhibit a superior methane production rate of 387.5 μmol•m^{-2}•h^{-1} (= c.a. 122.33 μmol•g^{-1}•h^{-1}) with an apparent quantum yield of c.a. 9.7% at 520 nm with engineered lengths. Moreover, 100% selective production toward CH$_4$ is also measured from the SnS/g-C$_3$N$_4$ photocatalysts, with > 10 h stable operation. These performances are, to the best of our knowledge, the highest production rate among reported photocatalytic films and metal sulfide/g-C$_3$N$_4$ composite-based photocatalysts. These highly improved performances are attributed to synergistic effects by the formation of nanostructured SnS/g-C$_3$N$_4$, exhibiting superior light absorption, higher crystallinity, Z-scheme charge transport via C-S bonding, physical advantages of the SnS nanostructure, and excellent physiochemical properties of the surfaces.

1. Introduction

Photocatalytic semiconductor system for CO$_2$ conversion to hydrocarbon fuels such as CH$_4$ is of great interest because that is an effective solution for the foreseeable energy crisis and ongoing environmental issues relating to > 30 Gt of massive CO$_2$ emission to the atmosphere annually [1]. The photocatalytic CO$_2$ conversion by semiconductor materials has been initiated by two monumental works done by Halmann in 1978 and Inoue et al. in 1979 [2,3]. Since these two works, lots of organic and inorganic semiconductor materials such as metal oxides (ex. TiO$_2$, ZnO, or WO$_3$), metal chalcogenides (ex. SnS$_2$, CdS, Bi$_2$S$_3$, and MoS$_x$), metal nitrides, conjugate polymers, and metal-organic frameworks have demonstrated their applicability to the photocatalytic system for CO$_2$ conversion [4-8].

Among these materials, graphitic carbon nitride (g-C$_3$N$_4$ or CN, here)

has been considered a promising n-type photocatalyst for CO$_2$ conversion since the successful demonstration by Wang et al. for hydrogen evolution under visible light in 2009 [9]. Not to mention advantages of the g-C$_3$N$_4$ material itself such as material stability, nontoxicity without any metal element, and facile synthesis process, g-C$_3$N$_4$ possesses great potential to be an efficient photocatalytic material for CO$_2$ conversion. g-C$_3$N$_4$ has a favorable band structure that brackets the redox potentials for CO$_2$ reduction and water oxidation reaction for CO$_2$ conversion. In addition, g-C$_3$N$_4$ has superior CO$_2$ adsorption ability via abundant NH and NH$_2$ functional groups at its surface. However, the limitation of available photons due to its wide bandgap (2.7 eV) and severe charge recombination (or short carrier lifetime of ~few ns) of g-C$_3$N$_4$ makes efficient and practical CO$_2$ conversion challenging [10,11]. In addition, g-C$_3$N$_4$-based photocatalysts are not favorable for the selective production of hydrocarbon species such as CH$_4$ which is a more practical type

for energy production.

To overcome the drawbacks of g- C_3N_4 and achieve a more practical CO_2 conversion for efficient and selective production of useful hydrocarbon species, various strategies have been explored in the aspects of materials and photocatalytic structure. Various strategies for performance enhancement have been explored in the aspects of materials and photocatalytic structure. For example, materials modification, the introduction of new morphology, and the formation of the junction with other materials for the improvement of efficient and selective CO_2 conversion have been attempted [12,13]. Forming a junction with other materials not only allows the use of the innate advantages of g-C_3N_4 but also additional features from the other materials and the interfaces made by the junction such as light absorption enhancement or more efficient charge separation [14]. Up to now, g-C_3N_4 has made successful junction structures with various semiconductor materials such as perovskite, metal oxides, and metal sulfides, showing improved light absorption from the smaller bandgap of other materials and enhanced charge separation properties through junction [15-17].

Tin (II) sulfide (SnS) is also one of the attractive p-type materials to form a junction with n-type g-C_3N_4 due to its excellent properties: material stability, abundance of the elements, nontoxicity, and excellent optical properties such as ~1.3 eV of optical band gap and $> 10^4$ cm^{-1} of absorption coefficient at the absorption edge [18]. These advantages have contributed to proving the applicability of SnS materials to photocatalytic structure [19-21]. However, bulk and intrinsic SnS materials do not have sufficient properties to achieve their efficient CO_2 conversion due to their own disadvantages, including the fast charge carrier recombination and the unfavorable charge transfer, which limits their photocatalytic efficiency [22,23]. Specifically, the bulk and intrinsic SnS materials have an unfavorable energy band position for water oxidation reaction and, because of this, it is believed that the SnS could not make a major contribution to the field of efficient water splitting and CO_2 conversion [24,25]. To tackle these limitations, material or structural modification has been suggested for the improvement of SnS properties [22,26,27]. Among those suggestions, the fabrication of one-dimensionally structured SnS is of special interest because it allows SnS to have unique properties that are different from those of the bulk and intrinsic SnS, such as strong light trapping via multiple light scattering, large specific area, fascinating electronic properties by quantum confinement and modification of electronic band structure [28,29]. In general, one-dimensionally structured SnS in nanorods (NRs) shape has been synthesized using a variety of methods including hydrothermal, solvothermal, ultrasonic, and electrodeposition methods as listed in Table S1. However, most of the fabricated SnS NRs are not shown in vertically grown shape, which might result in a loss of significant surface area and reaction sites for CO_2 conversion. Moreover, considering the configuration of a more practical photocatalytic system grown on a substrate, most of the synthesis methods are not suitable because synthesized SnS NRs are obtained in the form of powders and required another process for transfer to the substrates for their more practical usage. In this context, the sculptured thin films (STFs) technique can provide a convenient way of direct growth of nanostructures onto a substrate based on self-shadowing effect with controlled deposition conditions such as angle of vapor flux and substrate rotation [30].

Herein, for the first time, we demonstrate vertically grown SnS NRs directly on substrates and the formation of SnS NRs/g-C_3N_4 nanostructured photocatalysts for photocatalytic CO_2 conversion. The fabricated SnS NR/g-C_3N_4 photocatalysts show an extraordinary CH$_4$ production rate of 387.5 μmol•m^{-2}•h^{-1} (= c.a. 122.33 μmol•g^{-1}•h^{-1}) with > 10 h stable operation and an apparent quantum yield of c.a. 9.7% with 100% selectivity on CH$_4$ species. To the best of our knowledge, the performance achieved by our SnS NR/g-C_3N_4 photocatalysts is the best among the reported works for metal sulfide-based photocatalysts. These excellent achievements are investigated by systematic experiments and simulations in the various aspects: (1) material properties of SnS NR/g-C_3N_4 photocatalysts nanostructured material such as light absorption and crystallinity (2) charge transfer and charge availability for CO_2 reduction and water oxidation with the study on the energy band structure (3) physical advantages of the SnS nanostructure fabricated the STF technique, such as reaction sites and recombination (4) excellent physiochemical properties from the surfaces of SnS NR/g-C_3N_4 photocatalyst.

2. Experimental section

2.1. Materials

Urea (NH$_2$CONH$_2$, 99.0-100.5%, ACS reagent) was purchased from Alfa Aesar. Tin (II) sulfide (SnS, 99.999%) was obtained from I-MEI Materials. Potassium bicarbonate (KHCO$_3$, 99.7%, ACS reagent) was purchased from Sigma-Aldrich. Solvents, such as methanol, acetone, and isopropyl alcohol were of analytical grade.

2.2. Fabrication of the SnS/g-C_3N_4 photocatalysts

2.2.1. Fabrication of SnS nanostructured photocatalysts

The fabrication process of SnS nanostructured photocatalysts is illustrated in Fig. S1a. The SnS NRs were directly grown on a fluorine-doped tin oxide substrate (FTO) by a thermal evaporator. The FTO substrates were ultrasonically cleaned for 30 min using acetone, isopropyl alcohol, and deionized water in sequence. The cleaned substrates were dried using a nitrogen gun and kept inside the oven at 70 °C for 30 min. Prior to the NR growth process, the cleaned FTO substrates were treated with ozone for 30 min. For thermal evaporation, SnS powder was loaded into an alumina-coated tungsten boat, and the thermal evaporator chamber was pumped down to 1×10^{-6} Torr. The deposition rate was kept constant at 0.2 Å/s. The growth of the SnS NRs on substrates was implemented with 5° of the incident vapor flux angle. The deposited SnS NRs were annealed in a tube furnace at 300 °C with a ramping rate of 3 °C/min under an argon atmosphere. Then, the samples were cooled down to room temperature naturally. The fabricated SnS NR samples via STF technique were denoted as TSx, where x is the nominal film thickness from the quartz crystal thickness detector equipped in the thermal evaporator chamber, and x varied from 100 to 160 nm.

2.2.2. Synthesis of g-C_3N_4

g-C_3N_4 was prepared via one-step polymerization methods, which was reported in a previous report [31]. As shown in Fig. S2, 10 g of urea were put into an alumina crucible with a cover and dried in an oven at 80 °C for 12 h under ambient air. Subsequently, the crucible was heated in a tube furnace at 580 °C for 3 h with a heating rate of 3 °C/min. The powder was washed with nitric acid, deionized water, and ethanol to remove any residual alkaline species, then dried at 60 °C for 12 h.

2.2.3. Fabrication of SnS/g-C_3N_4 nanocomposite film

The decoration of g-C_3N_4 on the 1D SnS NR arrays was carried out via the dip coating method, which is reported in the literature [32], as shown in Fig. 1a and Fig. S1b. Firstly, 1 mg/mL of the g-C_3N_4 was ultrasonicated in methanol for 30 min. Secondly, the fabricated nanostructured SnS film was immersed in the g-C_3N_4 solution for 1 h and then dried at room temperature under an ambient atmosphere. The SnS/g-C_3N_4 nanocomposites were subsequently annealed at 300 °C for 1 h under Ar ambient with a heating rate 3 °C/min. The prepared SnS/g-C_3N_4 samples are denoted as TSx–CN depending on the nominal thickness of the SnS NRs.

2.3. Photocatalyst characterization

Field emission scanning electron microscope (FESEM, JEOL JSM-6700 F) and transmission electron microscope (TEM, JEOL 2100) were used to measure the morphology of the fabricated samples. High-resolution TEM (HR-TEM), scanning transmission electron microscopy
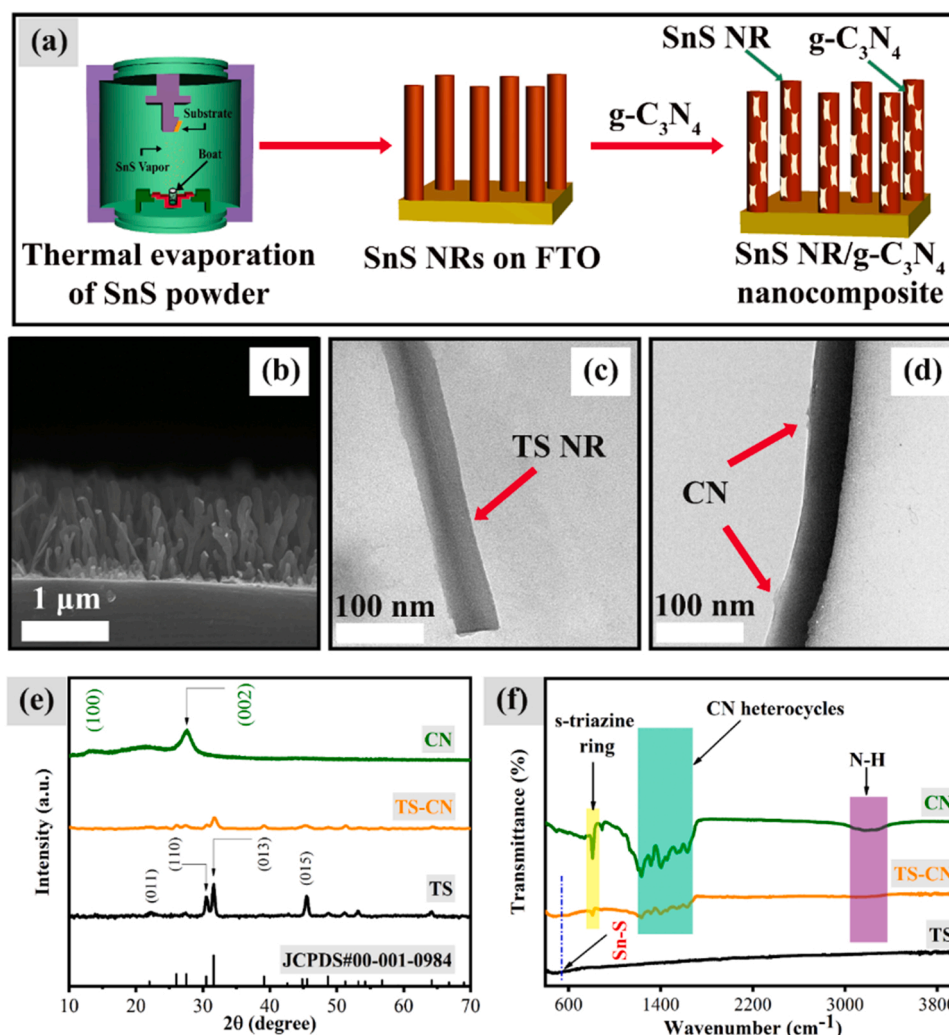
Fig. 1. (a) A schematic diagram of SnS NR/g-C$_3$N$_4$ photocatalysts fabricated by STF technique and dipping method (b) surface morphology of SnS NRs fabricated by STF technique via FE-SEM (c) TEM image for SnS NR and (d) g-C$_3$N$_4$-deposited SnS NR (e) X-ray diffraction patterns and (f) FT-IR spectra of CN, TS, and TS-CN samples.

(STEM), and EDX mapping were carried out using field emission TEM (FEG-TEM Tecnai F20 G2). The selected area electron diffraction (SAED) pattern was also taken by the field emission TEM. The crystallinities of all samples were measured by a multi-function X-ray diffractometer (XRD, Bruker D8). The chemical bonding was analyzed by Fourier-transform Infrared (FT-IR, Perkin Elmer-Frontier). The chemical composition of the synthesized photocatalysts was obtained from X-ray photoelectron spectroscopy (XPS, Thermo Scientific instrument with microfocused electron gun and multiposition aluminum anode). The X-ray absorption spectroscopy (XAS) was measured at beamline TPS 44 A and 20A1-Taiwan light source of the National Synchrotron Radiation Research Center facility in Taiwan. The C, N, and Sn K-edge were collected using fluorescence mode. The XAS spectra were plotted using the Athena program. The In-situ experiment was done inside a closed reactor with an open window sealed by Kapton tape. UV photoelectron spectroscopy (UPS) was measured for the study of the energy band structure. The optical properties of the samples were measured using a UV–vis spectrometer (Jasco J-1700 circular dichroism spectroscopy). The photoluminescence spectra were measured with a Fluoromax-4 spectrofluorometer (PL, Horiba). The electrochemistry measurements were carried out using an electrochemical station (CHI-6081E) with a three-electrode system. The CO$_2$-saturated solution was prepared with 0.1 M KHCO$_3$ in DI water. The photocatalyst film was taken as the working electrode. The Pt mesh and Ag/AgCl were used as counter electrode and reference electrode, respectively. Electrochemical impedance spectroscopy (EIS) measurement was carried out under dark conditions, and transient photocurrent (TPC) measurements were performed under AM 1.5 illumination (100 mW/cm^2). The experimental details for in-situ diffuse reflectance infrared Fourier transform spectroscopy (in situ DRIFTS) are provided in the supporting information (Section S1).

2.4. Photocatalytic CO$_2$ conversion reaction and performance measurement

The photocatalytic CO$_2$ conversion was implemented in a stainless-steel reactor of 25 mL volume equipped with a quartz window. The reaction was performed at ambient conditions (Room temperature and 1 atm) and under illumination of the solar simulator equipped with a 100 W Xe lamp and AM1.5 filter. For the reaction, the photocatalyst sample was placed at the bottom of the reactor. Prior to the light irradiation, the reactor was evacuated three times to remove the residual air inside the stainless-steel reactor by a mechanical pump. Subsequently, highly pure CO$_2$ (99.999%) was injected through a water bubbler with 9 mL of deionized water into the reactor at a rate of 4 mL/min to make an H$_2$O + CO$_2$ vapor mixture (~60% of relative humidity) as described in Fig. S3. The reactor was subsequently sealed, and a pressure of 1 atm was maintained during the experiment. After 2 h of continuous

radiation, 1 mL of the gaseous products were quantified by gas chromatography (GC-2030 Nexis; SHIMADZU system with Shincarbon ST Micropacked column, 80–100 mesh, 80 ℃) equipped with a barrier discharge ionization detector (BID-2030) at a temperature of 100 ℃.

The computational details are provided in the supporting information (Section S1).

## 3. Results and discussion

3.1. Characterization and material properties of SnS NR/g-C₃N₄ nanostructures

The morphology of the SnS films by the STF technique is demonstrated by FE-SEM in Fig. 1b and Fig. S4. The SnS is directly grown on the substrate and shows vertical nanorod (NR) shapes. The extended deposition time helped the length of the NRs to be grown up to > 1 μm

without any significant change in the morphology of SnS NR, showing ~30 nm of the averaged diameter regardless of their lengths in Fig. 1b and Fig. S5. The SnS NR/g-C₃N₄ samples were prepared with different thicknesses to grow different lengths of SnS NR for the experiment and named in the form of TSx-CN where, x = 100, 120, 140, and 160 nm from the thicknesses measured by the quartz crystal thickness detector of the evaporator. The measured lengths of the fabricated SnS NR samples are 411 nm, 450 nm, 493 nm, and 527 nm for TS100, TS120, TS140, and TS160 in Fig. S4, respectively. After the deposition of g-C₃N₄ by the dipping process on SnS NR, no remarkable difference in the surface morphology was found in Figs. 1c and 1d, other than the flake shape of g-C₃N₄, probably, owing to the small amount and/or thin thickness of the deposited g-C₃N₄.

Fig. 1e shows the X-ray diffraction patterns for g-C₃N₄ (CN), SnS NR (TS), and SnS NR/g-C₃N₄ (TS-CN) composite samples. CN displayed two distinct diffraction peaks at 2θ = 13.0° and 27.6° which can be assigned
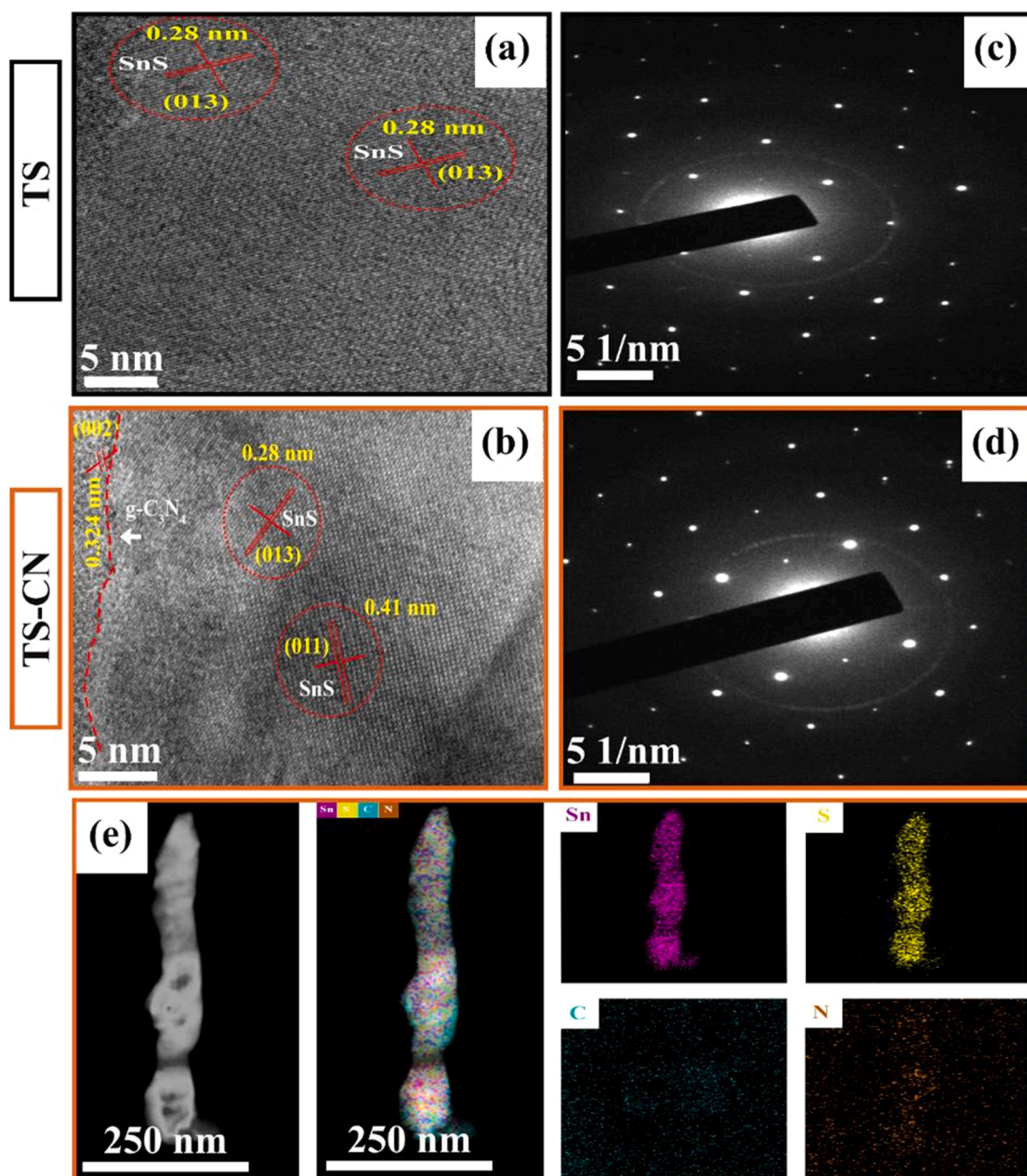

Fig. 2. Magnified TEM images of (a) TS and (b) TS-CN, SAED patterns of (c) TS and (d) TS-CN, (e) STEM image and corresponding EDS mapping of TS-CN nanocomposite for Sn, S, C, and N elements.

to the (100) and (002) crystal planes of CN, respectively [33]. The diffraction peaks at 13.0° and 27.6° are related to the in-planar tri-s--triazine units and the interlayer stacking of the conjugated systems with a distance of 0.324 nm for CN, respectively [33]. TS exhibits a set of intense diffraction peaks at 22°, 30.5°, 31.7°, and 45.6°, which correspond to the of (011), (110), (013), and (015), respectively, with the preferred growth orientation along the (013) plane. These peaks are indexed to the orthorhombic structure of SnS with lattice parameters of a = 3.94 Å, b = 4.34 Å, and c = 11.18 Å (JCPDS card number 00–001–0984). In the XRD measurement, no secondary peaks relating to SnS_2 and Sn_2S_3 phases were found [34,35]. After the deposition of g-C$_3$N$_4$ onto SnS NRs, the TS-CN sample exhibits decreased intensity from all the SnS characteristic peaks without the diffraction peaks at

13.0° and 27.6°. This probably results from the deposition of ultrathin g-C$_3$N$_4$ in a small amount on the SnS NRs via the dipping process as in the work reported by others [36]. The three samples were also examined with FT-IR in Fig. 1f. TS possesses the broad absorption peak located at ~540 cm^{-1} that is assigned for the vibration mode of the Sn–S bonding [37,38]. Except for this peak, TS has no other peaks relating to any adsorbed organic impurity such as C=C, C–H, C–O, C–S, and C=S species. CN shows the peak at 807 cm^{-1} that is indexed to out-of-plane breathing vibration of s-triazine units of CN as in other reports [33,39]. In addition, the four peaks at 1243, 1320, 1403, and 1560 cm^{-1} are assigned to the stretching vibration mode of the C–N heterocyclic ring of CN, and the strong peak at 1637 cm^{-1} is attributed to the C=N stretching vibration mode. TS-CN includes all characteristic peaks from
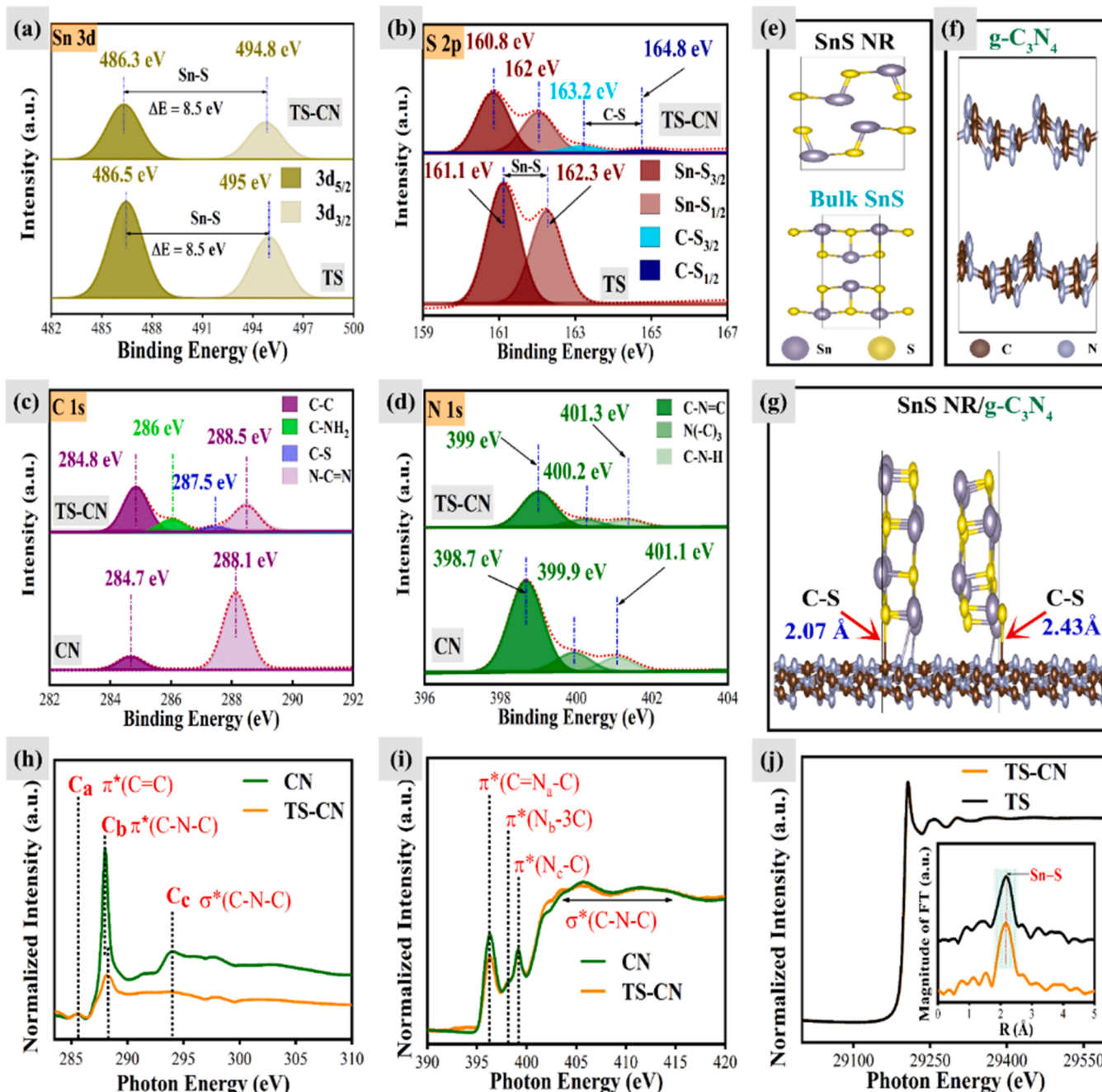
Fig. 3. HR-XPS spectra of Sn 3d (a), and S 2p (b) of TS and TS-CN catalysts. HR-XPS of C 1s (c) and N 1s (d) of CN and TS-CN. The simulation models of (e) individual bulk and nanostructured TS, (f) CN, and (g) TS-CN heterostructure. Synchrotron-based (h) C K-edge and (i) N K-edge XANES spectra for CN and TS-CN samples. (j) Synchrotron-based Sn K-edge XANES spectra for TS and TS-CN samples (the inset is EXAFS spectra of Sn K-edge).

TS and CN with decreased transmittance as shown in Fig. 1f and Fig. S6, further confirming the presence of g-C_3N_4 on the surface of SnS NRs as shown in the XRD results in Fig. 1e. Moreover, the new peak located at 1036 cm^{-1} could be attributed to the C-S stretching vibration as shown in Fig. S6b [40].

For further surface morphology investigation of the SnS NR and the g-C_3N_4/SnS NR nanocomposites, TEM measurement was implemented in Fig. 2. As mentioned in Fig. 1, there is no remarkable morphological change even with the decoration of g-C_3N_4 in the low-resolution TEM image. Figs. 2a and 2b show magnified images with clearly defined lattice fringe for TS and TS-CN, respectively. TS possesses the lattice fringes with an interplanar distance of 0.28 nm, which is in accordance with the XRD pattern of TS. For the TS-CN sample, 0.28 nm and 0.41 nm interplanar spacings are clearly observed in Fig. 2b, which correspond to (013) and (011) crystal planes of orthorhombic TS, respectively. In addition, the interplanar spacing of 0.324 nm was observed, again proving g-C_3N_4 with (002) plane forms a heterostructure with SnS NR via the dipping process. The corresponding SAED patterns in Figs. 2c and 2d confirmed the highly crystallized structure of TS and TS-CN samples. Fig. 2e shows the STEM image and the elemental mapping for Sn, S, C, and N elements. The Sn and S elements are highly concentrated and evenly dispersed distribution in the image, mimicking the morphology of the SnS NR while C and N elements show more scattered distribution, together with possible influence from the background. This suggests not only the presence of g-C_3N_4 materials but also the scattered distribution of the deposited g-C_3N_4 on the surface of the SnS NR, rather than forming a compact film. Moreover, the fabricated SnS NR exhibited nearly stoichiometric feature for SnS, suggesting that the sulfur loss during our thermal evaporation and post-annealing process in Ar ambient in Fig. S7 is moderate.

To further study the chemical composition and bonding configuration for TS, CN, and TS-CN, XPS measurement with the calibration using the C 1s core-level signal at 284.6 eV as a reference peak was implemented. Fig. S8 shows the survey spectra for TS, CN, and TS-CN in which all the major peaks, Sn 3d, S 2p, C 1s, and N 1s are measured. The high-resolution Sn 3d spectrum of TS in Fig. 3a exhibits two well-defined peaks at 486.3 eV and 494.8 eV which are assigned to Sn 3d$_{5/2}$ and Sn 3d$_{3/2}$, respectively. In addition, the energy difference between 3d$_{5/2}$ and 3d$_{3/2}$ is found to be 8.5 eV, which is consistent with the previous reports for SnS [41]. The S 2p spectrum in Fig. 3b reveals the two signature peaks positioned at 161.1 eV and 162.3 eV that are assigned to 2p$_{3/2}$ and 2p$_{1/2}$ of SnS. These results are also in good agreement with the previous reports [42,43]. After the decoration of the SnS NRs with g-C_3N_4, the peaks indexed to Sn 3d and S 2p were shifted to lower binding energies in Figs. 3a and 3b. In addition to the peak position shifts, the S 2p spectrum for TS-CN includes two new peaks at 163.2 eV and 164.8 eV. These two new peaks could be attributed to the formation of the C–S bond between SnS and g-C_3N_4 as in Fig. S6b [37,38]. Fig. 3c and Fig. 3d show the C 1s and N 1s spectrum for CN, respectively. The C 1s spectrum represents two peaks centered at 284.7 eV and 288.2 eV, which is attributed to sp^2 C–C bonds and sp^2-bonded carbon N–C=N, respectively [37,44]. The N 1s spectrum has three distinct peaks located at 398.7 eV, 399.9 eV, and 401.1 eV which are indexed for sp^2-bonded nitrogen C–N=C, tertiary nitrogen groups N(–C)$_3$, and amino groups (C–N–H), respectively. Interestingly, the presence of a new peak centered at 287.5 eV further confirms the formation of the C–S bond between g-C_3N_4 and SnS. In addition, after the formation of the TS-CN nanocomposite, the C 1s and N 1s spectra are shifted to higher energies, contrary to the case of Sn 3d and S 2p. Further study on C-S bonding is investigated via PBE with the DFT-D3 method as shown in Fig. 3e-g. The orthorhombic SnS NR is modeled with Pnma symmetry [45], differently from bulk SnS with Cmcm symmetry [46] as shown in Fig. 3e and Table S2. g-C_3N_4 has modeled a heptazine-based layer composed of six carbon and eight nitrogen atoms as shown in Fig. 3f, which is consistent with the literature [47]. The simulated SnS NR/g-C_3N_4 nanostructure in Fig. 3g qualitatively shows the formation of

a C-S bond with ~2.07–2.43 Å of the bonding lengths at interfaces as confirmed by FT-IR and XPS results.

The C K-edge X-ray absorption near edge structure (XANES) spectra in Fig. 3h show that both CN and TS-CN samples with three prominent features, donated as C$_a$, C$_b$, and C$_c$, which correspond to the out-of-plan excitation from C 1s to π * (C=C), the interlayer transition from C 1s to π*sp2 (N–C=N), and the 1s to σ * transition of C-N-C bonds, respectively. No obvious change is observed in the intensity and peak position of C$_a$ for CN and TS-CN, indicating that the SnS does not change the defective structure of the g-C_3N_4 framework [48]. Besides, the proximal absorption energy shift of the C$_b$ feature in the case of TS-CN compared with CN is consistent with the shift in the C 1s XPS spectra, confirming the presence of the C-S bonding between g-C_3N_4 and SnS [49]. The N K-edge spectra in Fig. 3i show the presence of three primary peaks located at ~ 396.3 (N$_a$), 398.3 (N$_b$), and 399.2 eV (N$_c$). The decreased intensity of the N$_a$ peak for TS-CN compared to the CN sample suggests the disturbance of C=N–C bonds by the newly introduced C-S interaction between SnS and g-C_3N_4. Moreover, the electronic configuration of Sn sites in the heterostructured catalyst was investigated via XANES technique. As shown in Fig. 3j, TS and TS-CN have nearly identical edge positions, illustrating that the valence state of Sn was unaffected by the deposition of g-C_3N_4 [50]. In addition, the overlapped spectra reveal that no interaction between SnS and g-C_3N_4 occurred on Sn atoms. The local atomic coordination environment of Sn atoms in the nanocomposite was illustrated by Fourier-transformed extended x-ray absorption fine structure (FT-EXAFS) of Sn K-edge as shown in the inset of Fig. 3j. Apparently, TS exhibits a distinct peak at 2.17 Å that is indexed to the Sn–S coordination. The slight shift in Sn–S distance along with the negligible change of intensity after decorating g-C_3N_4 could be attributed to the strong coupling between g-C_3N_4 and SnS at the interface as a result of interfacial C–S bond formation as confirmed by DFT simulations in Fig. 3g [51,52].

In the aspects of the formation of g-C_3N_4/SnS nanocomposites, two important findings must be focused on: the formation of the C-S bond and the shifts of the peaks after g-C_3N_4 decoration onto SnS NRs. The formation of the C-S bond proves that the g-C_3N_4 decoration through the dipping method here can provide a strong interaction between g-C_3N_4 and SnS and implies that g-C_3N_4/SnS nanocomposites possess a "bridge" for charge transfer [37,38]. Moreover, one of the major causes of the binding energy peak shifts after the formation of TS-CN results from the charge transfer between g-C_3N_4/SnS NR, possibly through the C-S bond. The charge transfer decreases the binding energy peaks for Sn 3d and S 2p and increases the ones for C 1s and N 1s. This proves the formation of pn heterojunction between g-C_3N_4/SnS NR through the C-S bond in our samples. This is advantageous for developing internal electric field (IEF) at the interface and this enables C-S bond and IEF-induced charge transport as in the previous report [53].

3.2. Photocatalytic CO_2 conversion performance of SnS NR/g-C_3N_4 nanostructures

The CO_2 conversion performance was evaluated for TS, CN, and TS-CN with varied lengths on SnS NRs in Fig. 4a. Sole TS has no detectable production rate for both CO and CH$_4$, while the prepared CN film photocatalyst can produce 360.8 and 132.8 μmol•m^{-2}•h^{-1} of CO and CH$_4$, respectively. However, with the decoration of g-C_3N_4 on the surface of SnS NRs, the TSx-CN photocatalysts immediately produce a high production rate of CH$_4$, and the production rate increases with increasing lengths of SnS NRs. The production rate recorded 387.5 μmol•m^{-2}•h^{-1} with 531 nm of SnS NRs (TS160-CN). Moreover, in spite of the presence of g-C_3N_4, all TSx-CN samples exhibit 100% selectivity toward CH$_4$ production. Further increase in lengths of SnS NRs with > 531 nm does not contribute to a significant improvement in CO_2 conversion performance.

The CH$_4$ production rate of 387.5 μmol•m^{-2}•h^{-1} from TS160-CN is, to the best of our knowledge, the highest production rate among the
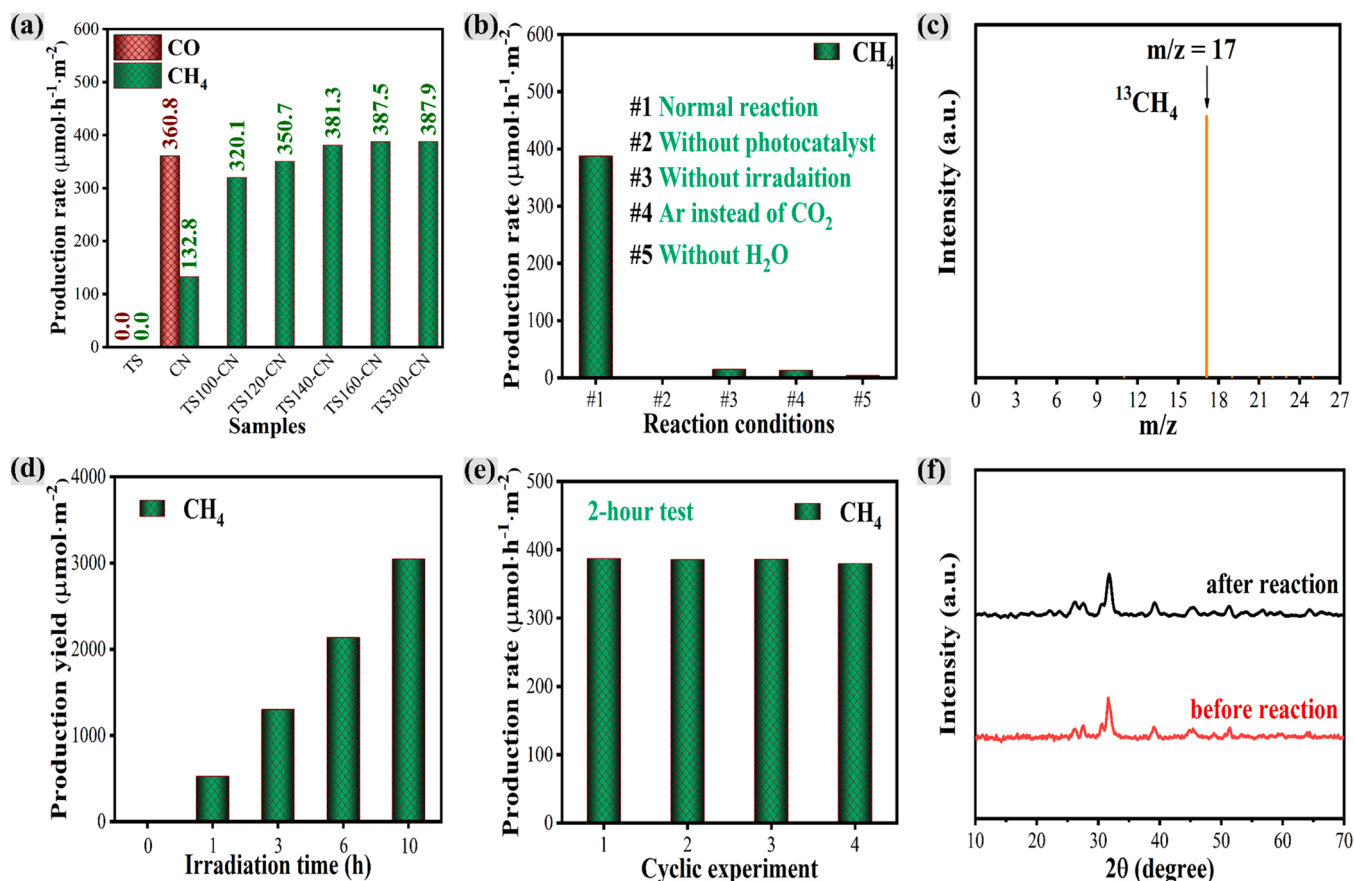
Fig. 4. (a) Production rates measured by various photocatalysts (b) CH_4 production rates of TS160-CN under various reaction conditions. (c) GC-Mass analysis of CH_4 using $^{13}CO_2$ for photocatalytic conversion over TS160-CN catalyst (d) CH_4 production yield of TS160-CN as a function of illumination time (e) recyclability test of TS160-CN over 2-hour photocatalytic reaction (f) XRD patterns of TS-CN composite film before and after four times photocatalytic CO_2 conversion.

photocatalytic films as listed in Table S3. This can be converted to the CH_4 production rate of c.a. 122.3 $\mu mol \bullet g^{-1} \bullet h^{-1}$ and the apparent quantum yield (AQY) of 9.7% at 520 nm that is calculated, following the reference [54]. To the best of our knowledge, this is the highest CH_4 production rate among $g\text{-}C_3N_4$ composite-based photocatalysts as listed in Table S4 and Table S5. Another feature is that our photocatalyst shows the selective production of CH_4, differently from other metal sulfides/$g\text{-}C_3N_4$ photocatalysts in Table S5 and Fig. S9.

To identify the reliability of the production rate measurement, the control experiments under different reaction conditions such as without photocatalyst, without irradiation, and with argon gas instead of CO_2, were implemented as in Fig. 4b. All the control experiments measured only a negligible amount of species, proving that the possible influence from carbon impurities or surface contamination is ignorable. Furthermore, in the absence of water, the photocatalytic reaction shows a negligible CO_2-to-CH_4 conversion, indicating that H_2O plays a crucial role as proton donors for CH_4 production. In addition, to confirm the origination of the measured CH_4, the measurement with isotopic $^{13}CO_2$ was performed during the photocatalytic reaction as shown in Fig. 4c. The produced CH_4 was detected by GC-MS and the signal at $m/z = 17$ proves that CO_2 is the main carbon source for the formation of CH_4 by our photocatalyst.

The continuous production and recyclability of the TS-CN photocatalysts are tested in Figs. 4d and 4e. TS160-CN photocatalyst produces a constant yield for CH_4 in terms of time with a mixture of CO_2 gas and water vapor under AM1.5 illumination. No remarkable decrease in the CH_4 yield was observed during a continuous 10 h reaction and the CH_4 yield reached 3046 $\mu mol \bullet m^{-2}$ after 10 h illumination. Fig. 4e represents the recyclability of TS160-CN photocatalyst under repetitive 2 h

illumination with refiled $CO_2 + H_2O$ vapor every 2 h. All four times measurements produce almost identical CH_4 production rate by TS160-CN photocatalyst and no degradation in the material was observed after the four-times measurement in Fig. 4e. These imply the excellent recyclability and stability of our photocatalyst. The stability of our SnS NR/$g\text{-}C_3N_4$ photocatalysts was examined via XRD, FT-IR, HR-XPS, XANES, and TEM techniques in structural, compositional, and morphological aspects as shown in Fig. 4f and Fig. S10. The nonremarkable changes in XRD, FT-IR, and XPS measurements after photocatalysis prove the structural and compositional stability against the CO_2 RR conditions, and almost identical Sn K-edge XANES spectra before and after photocatalytic CO_2 RR suggest that the valence state of Sn is stable. Moreover, the morphology of TS160-CN remains unchanged after photocatalytic CO_2 RR as shown by the TEM image in Fig. S10g. The appearance of SnS lattice fringes of the (013) crystal plane in the HR-TEM image (Fig. S10h) also indicates that the highly crystalline features of the catalyst remain after photocatalysis.

3.3. Optical and electrochemical properties of SnS NR/$g\text{-}C_3N_4$ nanostructures

To study the superior CO_2 conversion performance of our photocatalysts, the optical and electrochemical properties were measured by UV–vis spectroscopy, PL spectroscopy, transient photocurrent (TPC) measurement, and electrochemical spectroscopy in Fig. 5. Fig. 5a shows that CN has strong absorption only in shorter wavelengths, corresponding well with its band gap of 2.9 eV (Fig. S11) while TS shows more excellent absorption properties in extended wavelengths to visible light owing to its smaller bandgap of 1.57 eV (Fig. S12). The bandgap of
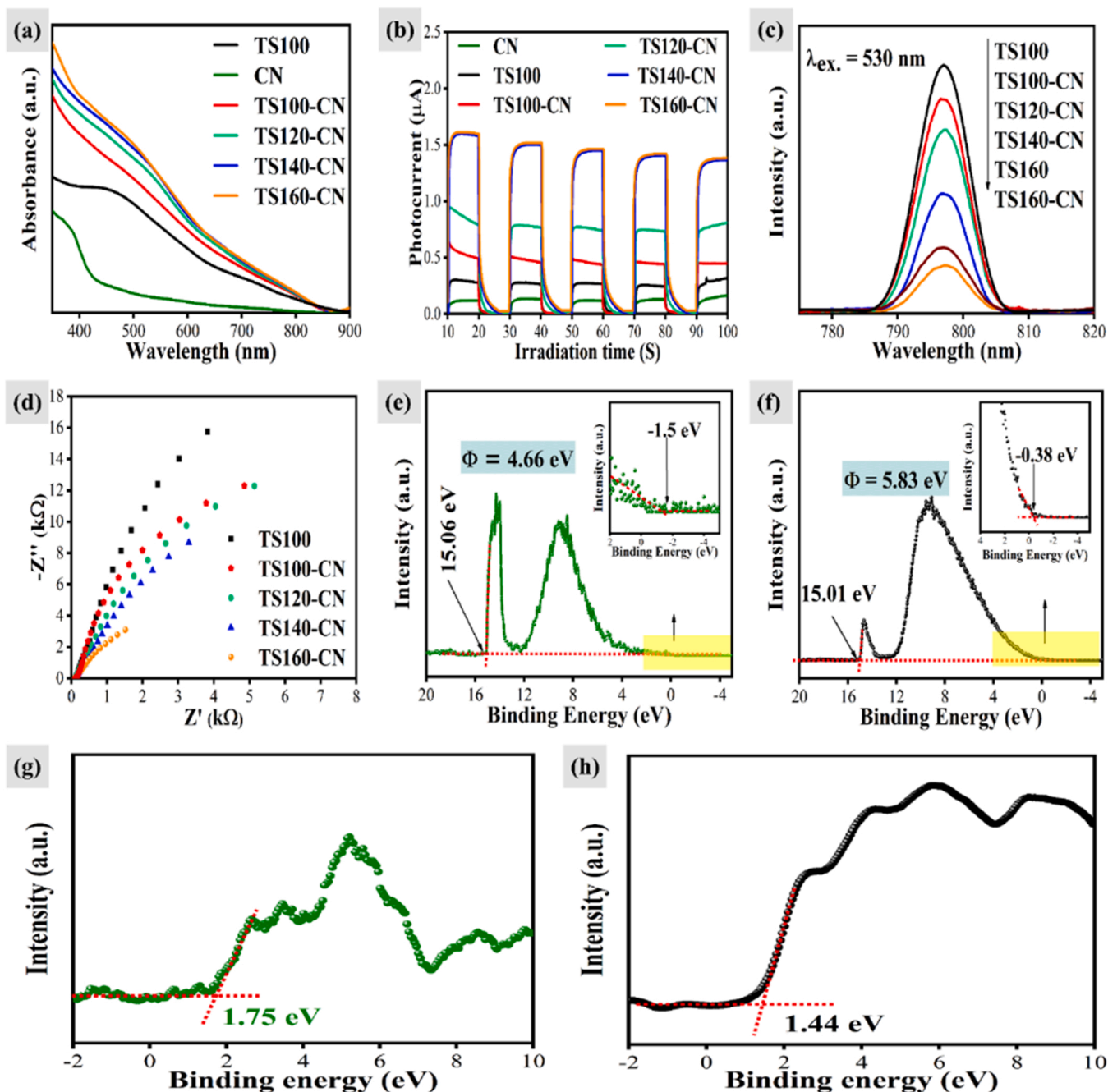
Fig. 5. (a) UV–vis absorption spectra and (b) transient photocurrent measurements of TS, CN, and TSx-CN samples (c) PL spectra of TS and TSx-CN nanocomposites by 530 nm wavelength excitation source (d) EIS spectra of TS and TS-CN nanocomposites in CO_2-saturated 0.1 M $KHCO_3$ solution measured under dark at 0.4 V of applied bias. UPS spectrum for (e) CN and (f) TS, VB-XPS spectrum for (g) CN and (h) TS.

1.57 eV for SnS NR is larger than that of the bulk SnS sample (1.24 eV in Fig. S13) owing to the quantum confinement effect induced by the formation of the one-dimensional nanostructured TS thin film [41]. These widened bandgaps are also confirmed from the density of states simulation results in Fig. S14 and Fig. S15. After the formation of TS-CN nanocomposites, a remarkable enhancement in absorbance is observed from all TSx-CN samples in entire measured wavelengths. However, TS160-CN exhibits nearly the same absorption spectrum as that of TS140-CN in spite of the increased length (493 nm →531 nm).

The same trend is observed with TPC results in Fig. 5b. All samples with SnS NRs show improved photocurrent in CO_2-saturated electrolyte in comparison with CN and TS100. In particular, the photocurrents generated by TS140-CN and TS160-CN are almost identical to those in

the absorbance spectrum. Fig. 5c is the photoluminescence spectrum with 530 nm of excitation light. A strong emission peak is measured at ~ 797 nm, which is attributed to the near band edge emission of SnS as reported in previous work [55]. The increased length and the decoration of g-C_3N_4 help for more efficient quenching of the PL intensity, and TS160-CN exhibits the most enhanced quenching capability. These results suggest the g-C_3N_4 decoration and the longer length of SnS NRs enable radiative recombination to be suppressed efficiently. In another aspect, these imply that the charge transfer from SnS NR to g-C_3N_4 occurs at g-C_3N_4/SnS NR and, owing to excellent charge transport ability through highly crystallized SnS NR, more g-C_3N_4/SnS NR interfaces are available for more efficient charge separation as depicted in Fig. S16. In addition, TSx-CN samples have superior characteristics in charge

transfer at the photocatalyst/CO_2 electrolyte interface in Fig. 5d. The diameter of the semicircle corresponds to the charge transfer resistance in the Nyquist plot [56]. All TSx-CN samples show improved charge transfer resistance, suggesting more efficient charge transfer from the photocatalyst to CO_2 species. Moreover, longer TSx-CN samples provide lower charge transfer resistance. Also, the TSx-CN samples exhibit more improved charge transfer resistance than that of CN (Fig. S17). It is speculated that this is related to the charge transfer when the SnS NR/g-C_3N_4 heterojunction is formed and results in band structure modification as shown in Fig. 3. The modified band structure of the photocatalyst allows the photocatalyst/CO_2 electrolyte interface to be more conductive. In addition, the longer TSx-CN would be more conductive due to more photocatalyst/CO_2 electrolyte interfaces.

In these contexts, the formation of TS-CN nanocomposites has

several advantages for the efficient and selective production of hydrocarbon fuels. First, 1.57 eV of the optical bandgap for the SnS NR enhances the light absorption and extends available photons up to ~800 nm of wavelengths for a higher production rate of solar fuels. Second, an enlarged number of electrons and a more intimate interface realize more selective production of CH_4 that requires more electrons and protons than CO for its formation. Third, the excellent charge transport characteristics of highly crystallized SnS NRs provide more efficient reaction sites for improved CO_2 conversion rate. Fourth, the engineered nanorod length of TS improves the effective surface area (see section S4 in the Supporting Information for estimating the surface area). All these advantages provide the synergistic effect for the conversion rate enhancement and selective production rate in Fig. 4.
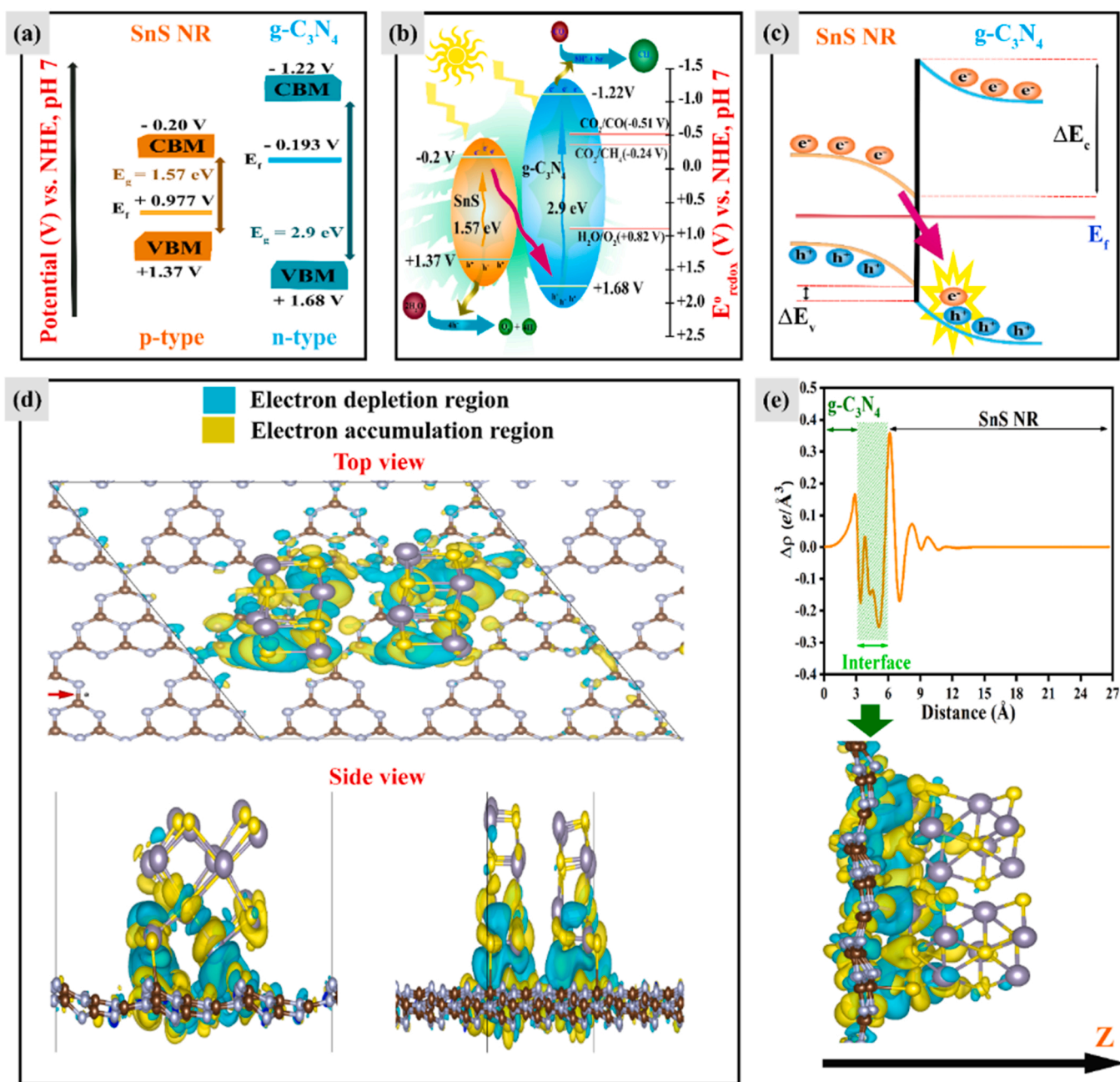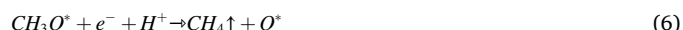

Fig. 6. Schematics of band structures for SnS NR and g-C_3N_4 (a) before and (b) after junction formation under illumination (c) at interface under illumination. ΔE_c, ΔE_v, and E_f stand for the conduction band offset, valence band offset, and Fermi level, respectively. (d) The top and side views of charge density difference at the TS-CN interface. (e) The planar averaged charge density difference for the TS-CN structure along the Z-scheme and the corresponding charge density alignments.

3.4. Proposed mechanism of efficient and selective CO₂ conversion by the SnS NR/g-C₃N₄ photocatalysts

In an attempt to establish the band structure of our TS-CN photocatalysts and to propose the underlying mechanism of the CO₂ conversion by the photocatalysts, the electronic band structure of our photocatalyst was studied with UPS and VB-XPS measurements, especially for CN and TS. Fig. 5e and Fig. 5f exhibit UPS spectra for g-C₃N₄ and SnS NR, respectively. Considering the width of the emitted electrons, W from UPS results, the work function, Φ is extracted from the following equation, Φ = 21.22 – W, where the He I photon energy is 21.22 eV [57]. The calculated work functions for CN and TS are 4.66 eV and 5.83 eV versus vacuum, respectively. In addition, the valence band density of states for TS and CN were investigated by VB-XPS in Fig. 5g and Fig. 5h to determine the valence band maximum (VBM) for the materials. The VBM of CN and TS is determined with band edges and the positions of VBM are 1.75 eV and 1.44 eV for CN and TS, respectively. These are again equivalent to 1.68 V and 1.37 V (Vs NHE) for CN and TS, respectively. In particular, 1.44 eV of VBM for SnS NR is more shifted down than that of bulk SnS (1.3 eV) in Fig. S18, which means the energy band structure of the SnS becomes more favorable for water oxidation owing to band structure modification by nanostructure formation [24, 25]. With the combination of the Tauc plot results in Fig. S11 and Fig. S12, the positions of the conduction band minimum (CBM) were obtained, and the positions of CBM are − 1.22 V and − 0.20 V (Vs NHE) for CN and TS, respectively.

Based on all the results from UPS, VB-XPS, and Tauc plots, the energy band structures of SnS NR and g-C₃N₄ before the formation of SnS NR and g-C₃N₄ nanocomposite Vs NHE at pH 7 are depicted as shown in Fig. 6a. After the deposition, p-type SnS NR forms a p-n heterojunction to n-type g-C₃N₄ through the C-S bond, and the resulted band diagram is described in Fig. 6b. In particular, the band structure of the SnS NR shows favorable to water oxidation and the favorable water adsorption by the SnS NR/g-C₃N₄ was confirmed by in situ XANES Sn K-edge spectra and the DFT calculation in Fig. S19a (see section S5 in the supporting Information). Due to the position of energy bands, the IEF is established at the SnS NR/g-C₃N₄ interface as described in Fig. 6c. The IEF directs the photogenerated carriers from SnS NR to g-C₃N₄. However, due to the conduction and valence band offsets (ΔE_c and ΔE_v, respectively), the photoelectrons from the SnS NR conduction band are transferred to the valence band of g-C₃N₄, following IEF and C-S bond modulated Z-scheme charge transfer mechanism. The following charge accumulation at the SnS NR/g-C₃N₄ interface is calculated in the yellow area in Fig. 6d, and the charge flow from SnS NR to g-C₃N₄ is simulated in Fig. 6e. This direction of the electron flow suppresses the electron recombination due to the annihilation of holes in the valance band in g-C₃N₄ and this makes more electron available for CO₂ reduction, together with more favorable CO₂ adsorption energy (E_{ads}= - 0.35 eV for SnS NR/g-C₃N₄ > E_{ads}= - 0.16 eV for g-C₃N₄ > E_{ads}= - 0.09 eV for SnS NR in Fig. S20a). Simultaneously, an ample amount of holes from SnS NR are available for vibrant H₂O oxidation by its modified band structure together with more favorable H₂O adsorption energy (E_{ads}= - 0.65 eV for SnS NR/g-C₃N₄ > E_{ads}= - 0.25 eV for SnS NR > E_{ads}= - 0.18 eV for g-C₃N₄ in Fig. S19a). Enhanced availability of electrons and holes from each side facilitates efficient CO₂ conversion to CH₄, instead of CO, which requires more numbers of electrons and holes for its production and this affects the CH₄ production rate and selectivity of the SnS NR/g-C₃N₄ photocatalysts, being coupled with enlarged reaction sites by the incorporation of nanostructure and improved light harvest by the smaller bandgap of SnS NR as shown in Fig. 4a. In addition, the desorption energy of the SnS NR/g-C₃N₄ (E_{des}= + 0.07 eV) is more favorable for CH₄ while the one of g-C₃N₄ is more favorable for CO. This also probably contribute to selective and efficient CH₄ production by the SnS NR/g-C₃N₄ photocatalysts [58]. More detailed and additional explanation on the selectivity by the SnS NR/g-C₃N₄ photocatalyst are provided in Section S6 in the Supporting Information. Furthermore, the reaction pathway for CH₄ production was speculated by in-situ DRIFTS measurements for our photocatalyst in Fig. S20b. Confirming CHO and CH₃O intermediates during CO₂ conversion, the reaction pathway is presumably followed by previous report as below (see Section S6 for more details in the Supporting Information)[59]:

$$* + CO_2 + e^- + H^+ \rightarrow COOH^* \tag{1}$$

$$COOH^* + e^- + H^+ \rightarrow CO^* + H_2O \tag{2}$$

$$CO^* + e^- + H^+ \rightarrow CHO^* \tag{3}$$

$$CHO^* + e^- + H^+ \rightarrow CH_2O^* \tag{4}$$

$$CH_2O^* + e^- + H^+ \rightarrow CH_3O^* \tag{5}$$

$$CH_3O^* + e^- + H^+ \rightarrow CH_4\uparrow + O^* \tag{6}$$

$$O^* + e^- H^+ \rightarrow OH^* \tag{7}$$

$$OH^* + e^- + H^+ \rightarrow H_2O + O^* \tag{8}$$

where the asterisks indicate catalytically active sites.

4. Conclusion

In this work, we demonstrated a SnS/g-C₃N₄ nanostructured photocatalyst for efficient and selective CO₂ conversion to methane. The thermally evaporated SnS is directly grown on substrates in a vertical nanorod structure. Through the facile dipping process, the SnS nanorod formed a p-n heterojunction by the formation of C-S bonding. The SnS/g-C₃N₄ nanostructured photocatalyst produced the CH₄ production rate of 387.5 μmol•m⁻²•h⁻¹ (= c.a. 122.3 μmol•g⁻¹•h⁻¹) the apparent quantum yield (AQY) of c.a. 9.7% at 520 nm from TS160-CN is, to the best of our knowledge, the highest production rate among photocatalytic films and metal sulfide/g-C₃N₄ composite-based photocatalysts, with 100% selectivity toward CH₄. In addition, the fabricated SnS NR/g-C₃N₄ photocatalysts showed stable CO₂ conversion for > 10 h operation. These highly improved performances are attributed to synergistic effects by the formation of SnS NR/g-C₃N₄: (1) superior material properties of SnS nanostructured material such as excellent light absorption and high crystallinity (2) efficient charge transfer and ample charge availability for CO₂ reduction and water oxidation by Z-scheme charge transfer through C-S bonding and induced IEF (3) physical advantages of the SnS nanostructure fabricated the STF technique, such as improved numbers of reaction sites and suppressed recombination (4) excellent physiochemical properties of the surfaces of SnS NR/g-C₃N₄ photocatalyst. This works provides a systematic and profound understanding of nanostructured photocatalysts and their reactions for the efficient CO₂ conversion and we believe this would contribute to the realization of more practical CO₂ conversion for the industry and our environment.

CRediT authorship contribution statement

H. A. E. Omr: Conceptualization, Visualization, Investigation, Methodology, Formal analysis, Data curation, Writing – original draft, Writing – review & editing. **R. Putikam:** Investigation, Methodology, Data curation, Writing – review & editing. **M. K. Hussien:** Investigation, Methodology, Data curation, Writing – review & editing, **A. Sabbah:** Investigation, Methodology, Data curation, Writing – review & editing. **T.Y Lin:** Investigation, Methodology, Data curation. **K.H. Chen:** Investigation, Writing – review & editing, Resources. **H.L Wu:** Investigation, Writing – review & editing, Resources. **S.P Feng:** Investigation, Writing – review & editing. **M.C. Lin:** Investigation, Writing – review & editing **H. Lee:** Conceptualization, Investigation, Data curation, Writing – review & editing, Supervision, Funding acquisition, Project

administration, Validation, Resources.

Declaration of Competing Interest

The authors declare that they have no known competing financial interests or personal relationships that could have appeared to influence the work reported in this paper.

Data availability

Data will be made available on request.

Acknowledgments

Appendix A. Supporting information

Supplementary data associated with this article can be found in the online version at doi:10.1016/j.apcatb.2022.122231.

References

[1] B. Li, Y. Duan, D. Luebke, B. Morreale, Advances in CO_2 capture technology: a patent review, Appl. Energy 102 (2013) 1439–1447.

[2] M. Halmann, Photoelectrochemical reduction of aqueous carbon dioxide on p-type gallium phosphide in liquid junction solar cells, Nature 275 (1978) 115–116.

[3] T. Inoue, A. Fujishima, S. Konishi, K. Honda, Photoelectrocatalytic reduction of carbon dioxide in aqueous suspensions of semiconductor powders, Nature 277 (1979) 637–638.

[5] Y.Y. Lee, H.S. Jung, Y.T. Kang, A review: Effect of nanostructures on photocatalytic CO_2 conversion over metal oxides and compound semiconductors, J. CO_2 Util. 20 (2017) 163–177.

[7] J. Wang, S. Lin, N. Tian, T. Ma, Y. Zhang, H. Huang, Nanostructured metal sulfides: classification, modification strategy, and solar-driven CO_2 reduction application, Adv. Funct. Mater. 31 (2021), 2008008.

[4] J. Di, C. Chen, C. Zhu, P. Song, M. Duan, J. Xiong, R. Long, M. Xu, L. Kang, S. Guo, Cobalt nitride as a novel cocatalyst to boost photocatalytic CO_2 reduction, Nano Energy 79 (2021), 105429.

[8] C. Yang, W. Huang, L.C. da Silva, K.A. Zhang, X. Wang, Functional conjugated polymers for CO_2 reduction using visible light, Chem. Eur. J. 24 (2018) 17454–17458.

[6] D. Li, M. Kassymova, X. Cai, S.-Q. Zang, H.-L. Jiang, Photocatalytic CO_2 reduction over metal-organic framework-based materials, Coord. Chem. Rev. 412 (2020), 213262.

[9] X. Wang, K. Maeda, A. Thomas, K. Takanabe, G. Xin, J.M. Carlsson, K. Domen, M. Antonietti, A metal-free polymeric photocatalyst for hydrogen production from water under visible light, Nat. Mater. 8 (2009) 76–80.

[10] S. Cao, J. Low, J. Yu, M. Jaroniec, Polymeric photocatalysts based on graphitic carbon nitride, Adv. Mater. 27 (2015) 2150–2176.

[11] Z. Sun, H. Wang, Z. Wu, L. Wang, g-C_3N_4 based composite photocatalysts for photocatalytic CO_2 reduction, Catal. Today 300 (2018) 160–172.

[13] P. Xia, B. Zhu, J. Yu, S. Cao, M. Jaroniec, Ultra-thin nanosheet assemblies of graphitic carbon nitride for enhanced photocatalytic CO_2 reduction, J. Mater. Chem. A 5 (2017) 3230–3238.

[12] H. Shi, S. Long, S. Hu, J. Hou, W. Ni, C. Song, K. Li, G.G. Gurzadyan, X. Guo, Interfacial charge transfer in 0D/2D defect-rich heterostructures for efficient solar-driven CO_2 reduction, Appl. Catal. B 245 (2019) 760–769.

[14] H.A. Omr, M.W. Horn, H. Lee, Low-dimensional nanostructured photocatalysts for efficient CO_2 conversion into solar fuels, Catalysts 11 (2021) 418.

[16] M. Ou, W. Tu, S. Yin, W. Xing, S. Wu, H. Wang, S. Wan, Q. Zhong, R. Xu, Amino-assisted anchoring of $CsPbBr_3$ perovskite quantum dots on porous g-C_3N_4 for enhanced photocatalytic CO_2 reduction, Angew. Chem. 130 (2018) 13758–13762.

[17] Y. Wang, H.S. Jung, J. Mei, S. Sarina, Z. Wu, T. Liao, C. Yan, Z. Sun, Strongly interfacial-coupled ^{2}D–^{2}D TiO_2/g-C_3N_4 heterostructure for enhanced visible-light induced synthesis and conversion, J. Hazard. Mater. 394 (2020), 122529.

[15] X. Hao, J. Zhou, Z. Cui, Y. Wang, Y. Wang, Z. Zou, Zn-vacancy mediated electron-hole separation in ZnS/g-C_3N_4 heterojunction for efficient visible-light photocatalytic hydrogen production, Appl. Catal. B 229 (2018) 41–51.

[18] R. Banai, M. Horn, J. Brownson, A review of tin (II) monosulfide and its potential as a photovoltaic absorber, Sol. Energy Mater. Sol. Cells 150 (2016) 112–129.

[19] S. Jayswal, R.S. Moirangthem, Construction of a solar spectrum active SnS/ZnO p–n heterojunction as a highly efficient photocatalyst: the effect of the sensitization process on its performance, N. J. Chem. 42 (2018) 13689–13701.

[20] S. Juntrapirom, D. Tantraviwat, S. Suntalelat, O. Thongsook, S. Phanichphant, B. Inceesungvorn, Visible light photocatalytic performance and mechanism of highly efficient SnS/BiOI heterojunction, J. Colloid Interface Sci. 504 (2017) 711–720.

[21] M. Liang, T. Borjigin, Y. Zhang, H. Liu, B. Liu, H. Guo, Z-scheme Au@ Void@ g-C_3N_4/SnS yolk–shell heterostructures for superior photocatalytic CO_2 reduction under visible light, ACS Appl. Mater. Interfaces 10 (2018) 34123–34131.

[23] A. Polizzotti, A. Faghaninia, J.R. Poindexter, L. Nienhaus, V. Steinmann, R.L. Hoye, A. Felten, A. Deyine, N.M. Mangan, J.P. Correa-Baena, Improving the carrier lifetime of tin sulfide via prediction and mitigation of harmful point defects, J. Phys. Chem. Lett. 8 (2017) 3661–3667.

[22] T. Jia, F. Fu, J. Li, Z. Deng, F. Long, D. Yu, Q. Cui, W. Wang, Rational construction of direct Z-scheme SnS/g-C_3N_4 hybrid photocatalyst for significant enhancement of visible-light photocatalytic activity, Appl. Surf. Sci. 499 (2020), 143941.

[25] C.-Y. Wu, C.-J. Lee, Y.-H. Yu, H.-W. Tsao, Y.-H. Su, C.-C. Kaun, J.-S. Chen, J.-J. Wu, Efficacious CO_2 photoconversion to C2 and C3 hydrocarbons on upright SnS–SnS_2 heterojunction nanosheet frameworks, ACS Appl. Mater. Interfaces 13 (2021) 4984–4992.

[24] X. Li, X. Zuo, X. Jiang, D. Li, B. Cui, D. Liu, Enhanced photocatalysis for water splitting in layered tin chalcogenides with high carrier mobility, Phys. Chem. Chem. Phys. 21 (2019) 7559–7566.

[26] V. Steinmann, R. Jaramillo, K. Hartman, R. Chakraborty, R.E. Brandt, J. R. Poindexter, Y.S. Lee, L. Sun, A. Polizzotti, H.H. Park, 3.88% efficient tin sulfide solar cells using congruent thermal evaporation, Adv. Mater. 26 (2014) 7488–7492.

[27] G.K. Veerasubramani, M.-S. Park, J.-Y. Choi, D.-W. Kim, Ultrasmall SnS quantum dots anchored onto nitrogen-enriched carbon nanospheres as an advanced anode material for sodium-ion batteries, ACS Appl. Mater. Interfaces 12 (2020) 7114–7124.

[29] J. Zhou, Y. Li, L. Yu, Z. Li, D. Xie, Y. Zhao, Y. Yu, Facile in situ fabrication of Cu_2O@Cu metal-semiconductor heterostructured nanorods for efficient visible-light driven CO_2 reduction, Chem. Eng. J. 385 (2020), 123940.

[28] T. Jin, Q. Han, Y. Wang, L. Jiao, 1D nanomaterials: design, synthesis, and applications in sodium–ion batteries, Small 14 (2018), 1703086.

[30] A. Barranco, A. Borras, A.R. Gonzalez-Elipe, A. Palmero, Perspectives on oblique angle deposition of thin films: from fundamentals to devices, Prog. Mater. Sci. 76 (2016) 59–153.

[31] Y. Zhang, J. Liu, G. Wu, W. Chen, Porous graphitic carbon nitride synthesized via direct polymerization of urea for efficient sunlight-driven photocatalytic hydrogen production, Nanoscale 4 (2012) 5300–5303.

[32] J. Safaei, N.A. Mohamed, M.F.M. Noh, M.F. Soh, N.A. Ludin, M.A. Ibrahim, W.N.R. W. Isahak, M.A.M. Teridi, Graphitic carbon nitride (g-C_3N_4) electrodes for energy conversion and storage: a review on photoelectrochemical water splitting, solar cells and supercapacitors, J. Mater. Chem. A 6 (2018) 22346–22380.

[33] S. Zhou, Y. Liu, J. Li, Y. Wang, G. Jiang, Z. Zhao, D. Wang, A. Duan, J. Liu, Y. Wei, Facile in situ synthesis of graphitic carbon nitride (g-C_3N_4)-N-TiO_2 heterojunction as an efficient photocatalyst for the selective photoreduction of CO_2 to CO, Appl. Catal. B 158 (2014) 20–29.

[34] T. Billo, I. Shown, A. kumar Anbalagan, T.A. Effendi, A. Sabbah, F.-Y. Fu, C.-M. Chu, W.-Y. Woon, R.-S. Chen, C.-H. Lee, A mechanistic study of molecular CO_2 interaction and adsorption on carbon implanted SnS_2 thin film for photocatalytic CO_2 reduction activity, Nano Energy 72 (2020), 104717.

[35] C. Xue, X. Yan, H. An, H. Li, J. Wei, G. Yang, Bonding CdS-Sn_2S_3 eutectic clusters on graphene nanosheets with unusually photoreaction-driven structural reconfiguration effect for excellent H_2 evolution and Cr (VI) reduction, Appl. Catal. B 222 (2018) 157–166.

[36] M. Wang, M. Shen, L. Zhang, J. Tian, X. Jin, Y. Zhou, J. Shi, ^{2}D–^{2}D MnO_2/g-C_3N_4 heterojunction photocatalyst: in-situ synthesis and enhanced CO_2 reduction activity, Carbon 120 (2017) 23–31.

[38] A. Zhu, L. Qiao, Z. Jia, P. Tan, Y. Liu, Y. Ma, J. Pan, C–S bond induced ultrafine SnS_2 dot/porous g-C_3N_4 sheet 0D/2D heterojunction: synthesis and photocatalytic mechanism investigation, Dalton Trans. 46 (2017) 17032–17040.

[37] Z. Zhang, J. Huang, M. Zhang, Q. Yuan, B. Dong, Ultrathin hexagonal SnS_2 nanosheets coupled with g-C_3N_4 nanosheets as 2D/2D heterojunction photocatalysts toward high photocatalytic activity, Appl. Catal. B 163 (2015) 298–305.

[39] Y. Xu, X. Jin, T. Ge, H. Xie, R. Sun, F. Su, X. Li, L. Ye, Realizing efficient CO_2 photoreduction in Bi_3O_4Cl: Constructing van der Waals heterostructure with g-C_3N_4, Chem. Eng. J. 409 (2021), 128178.

[40] J. Zhao, M. Ji, H. Chen, Y.-X. Weng, J. Zhong, Y. Li, S. Wang, Z. Chen, J. Xia, H. Li, Interfacial chemical bond modulated $Bi_{19}S_{27}Br_3$/g-C_3N_4 Z-scheme heterojunction for enhanced photocatalytic CO_2 conversion, Appl. Catal. B 307 (2022), 121162.

[41] S.R. Suryawanshi, S.S. Warule, S.S. Patil, K.R. Patil, M.A. More, Vapor–liquid–solid growth of one-dimensional tin sulfide (SnS) nanostructures with promising field emission behavior, ACS Appl. Mater. Interfaces 6 (2014) 2018–2025.

[43] M. Steichen, R. Djemour, L. Gütay, S. Siebentritt, P.J. Dale, Direct synthesis of single-phase p-type SnS by electrodeposition from a dicyanamide ionic liquid at high temperature for thin film solar cells, J. Phys. Chem. C 117 (2013) 4383–4393.

[42] A. Rauf, M.S.A.S. Shah, J.Y. Lee, C.-H. Chung, J.W. Bae, P.J. Yoo, Non-stoichiometric SnS microspheres with highly enhanced photoreduction efficiency for Cr (VI) ions, RSC Adv. 7 (2017) 30533–30541.

[44] X. Zhang, J. Yan, F. Zheng, J. Zhao, L.Y.S. Lee, Designing charge transfer route at the interface between WP nanoparticle and g-C_3N_4 for highly enhanced photocatalytic CO_2 reduction reaction, Appl. Catal. B 286 (2021), 119879.

[45] J.M. Skelton, L.A. Burton, A.J. Jackson, F. Oba, S.C. Parker, A. Walsh, Lattice dynamics of the tin sulphides SnS_2, SnS and Sn_2S_3: vibrational spectra and thermal transport, Phys. Chem. Chem. Phys. 19 (2017) 12452–12465.

[46] U. Aseginolaza, R. Bianco, L. Monacelli, L. Paulatto, M. Calandra, F. Mauri, A. Bergara, I. Errea, Strong anharmonicity and high thermoelectric efficiency in high-temperature SnS from first principles, Phys. Rev. B 100 (2019) 214307.

[47] J. Wang, D. Hao, J. Ye, N. Umezawa, Determination of crystal structure of graphitic carbon nitride: ab initio evolutionary search and experimental validation, Chem. Mater. 29 (2017) 2694–2707.

[48] M.K. Hussien, A. Sabbah, M. Qorbani, M.H. Elsayed, P. Raghunath, T.-Y. Lin, S. Quadir, H.-Y. Wang, H.-L. Wu, D.-L.M. Tzou, Metal-free four-in-one modification of g-C$_3$N$_4$ for superior photocatalytic CO$_2$ reduction and H$_2$ evolution, Chem. Eng. J. 430 (2022), 132853.

[49] Y. Wang, Y. Zhang, Y. Wang, C. Zeng, M. Sun, D. Yang, K. Cao, H. Pan, Y. Wu, H. Liu, Constructing van der waals heterogeneous photocatalysts based on atomically thin carbon nitride sheets and graphdiyne for highly efficient photocatalytic conversion of CO$_2$ into CO, ACS Appl. Mater. Interfaces 13 (2021) 40629–40637.

[50] J. Jiang, D. Duan, J. Ma, Y. Jiang, R. Long, C. Gao, Y. Xiong, Van der waals heterostructures by single cobalt sites-anchored graphene and g-C$_3$N$_4$ nanosheets for photocatalytic syngas production with tunable CO/H$_2$ ratio, Appl. Catal. B 295 (2021), 120261.

[51] J. Bai, T. Meng, D. Guo, S. Wang, B. Mao, M. Cao, Co$_9$S$_8$@ MoS$_2$ core–shell heterostructures as trifunctional electrocatalysts for overall water splitting and Zn–air batteries, ACS Appl. Mater. Interfaces 10 (2018) 1678–1689.

[52] W. Yao, W. Zheng, J. Xu, C. Tian, K. Han, W. Sun, S. Xiao, ZnS-SnS@ NC Heterostructure as robust lithiophilicity and sulfiphilicity mediator toward high-rate and long-life lithium–sulfur batteries, ACS nano 15 (2021) 7114–7130.

[53] X. Wang, X. Wang, J. Huang, S. Li, A. Meng, Z. Li, Interfacial chemical bond and internal electric field modulated Z-scheme Sv-ZnIn$_2$S$_4$/MoSe$_2$ photocatalyst for efficient hydrogen evolution, Nature, Communications 12 (2021) 1–11.

[54] S. Sorcar, Y. Hwang, C.A. Grimes, S.-I. In, Highly enhanced and stable activity of defect-induced titania nanoparticles for solar light-driven CO$_2$ reduction into CH$_4$, Mater. Today 20 (2017) 507–515.

[55] A. Arulanantham, S. Valanarasu, K. Jeyadheepan, A. Kathalingam, Effect of carrier gas pressure on structural, optical and photovoltaic properties of tin sulphide thin films prepared by nebulizer spray pyrolysis method, Bull. Mater. Sci. 42 (2019) 1–13.

[56] L. Huang, B. Li, B. Su, Z. Xiong, C. Zhang, Y. Hou, Z. Ding, S. Wang, Fabrication of hierarchical Co$_3$O$_4$@CdIn$_2$S$_4$ p–n heterojunction photocatalysts for improved CO$_2$ reduction with visible light, J. Mater. Chem. A 8 (2020) 7177–7183.

[57] Y.E. Ha, G.E. Lim, M.Y. Jo, J. Park, Y.-C. Kang, S.-J. Moon, J.H. Kim, Enhancing the efficiency of opto-electronic devices by the cathode modification, J. Mater. Chem. C. 2 (2014) 3820–3825.

[58] J. Fu, K. Jiang, X. Qiu, J. Yu, M. Liu, Product selectivity of photocatalytic CO$_2$ reduction reactions, Mater. Today 32 (2020) 222–243.

[59] X. Li, Y. Sun, J. Xu, J. Shao, J. Wu, X. Xu, Y. Pan, H. Ju, J. Zhu, Y. Xie, Selective visible-light-driven photocatalytic CO$_2$ reduction to CH$_4$ mediated by atomically thin CuIn$_5$S$_8$ layers, Nat. Energy 4 (2019) 690–699.